Radiative heating of low-Z solid foils by laser-generated x rays

K. Eidmann, I. B. Földes,* Th. Löwer, J. Massen, R. Sigel, G. D. Tsakiris, and S. Witkowski
Max-Planck-Institut für Quantenoptik, D-85740 Garching, Germany

H. Nishimura, Y. Kato, T. Endo,† H. Shiraga, M. Takagi, and S. Nakai
Institute of Laser Engineering, Osaka University, Suita Osaka, 565 Japan
(Received 26 May 1995)

The x-ray emission and burnthrough of radiatively heated low-Z plastic foils (C_8H_8, nCH_2, or CF_2) have been investigated in gold cavities of different shape and size, which were heated by the Gekko XII laser up to a radiation brightness temperature of 160 eV. The cavity radiation temperatures were obtained spectroscopically as well as from the speed of the shock that is radiatively driven into aluminum. From measured carbon burnthrough spectra we derived mass ablation rates at drive temperatures ranging from 100 to 180 eV. In addition we measured temporally resolved reemission spectra of carbon. The time- and frequency-integrated reemission was 23% of the gold reemission or 16% when normalized to the driving cavity flux. The measurements are in good agreement with numerical hydrodynamic computer code simulations based on multigroup radiation diffusion.

PACS number(s): 52.50.Jm, 44.40.+a, 52.25.Nr, 32.30.Rj

I. INTRODUCTION

High-power laser light focused on high-Z targets is efficiently converted into soft x rays. Simple converters are planar massive gold targets [1,2] or thin gold foil converters [3–5], which convert a considerable fraction (up to about 80%) of the laser energy into x-ray energy. By using *Hohlraum* targets, i.e., by heating with the laser the interior of millimeter-size gold cavities, nearly thermal isotropic x rays with intensities of up to 10^{15} W/cm^2 corresponding to radiation temperatures up to 300 eV have been generated [6,7]. If solid matter is irradiated by these intense x rays, they propagate into the wall under the influence of the decreasing opacity due to the heating and ionization of the matter. The result is the formation of a radiative heat wave, which transforms the matter into a hot dense plasma [8–10]. The advantage of this so-called radiative heating compared to direct heating with the laser is the high uniformity that can be achieved. This is caused by the incoherent nature of the thermal x rays resulting in a nicely uniform spatial intensity distribution and by the fact that the x rays penetrate deeply into the solid, thus heating regions of high density. In contrast, the laser beam may suffer from spatial nonuniformity. Also, it is absorbed at the critical density much below the solid density resulting in stronger temperature and density gradients.

Radiative heating is of fundamental importance for studying dense hot matter. It allows one to measure x-ray opacities in a range of astrophysical relevance [11,12] or to investigate the equation of state by generating extremely uniform high-pressure shock waves [13,14]. Moreover, the uniform ablation attainable by radiative heating is the key issue of indirect drive inertial confinement fusion (ICF), where the capsule is imploded by the intense x rays created in a *Hohlraum* [15]. The wall of the capsule (in contrast to the high-Z wall of the *Hohlraum)* has to consist of low-Z material, which absorbs the incident x rays efficiently because of its low reemission [16]. It is crucial for this application to know how the radiation transport evolves in the low-Z wall of the capsule. Besides the basic properties, such as the temperature and the density of the heated wall, it is important to know how fast the heat wave penetrates into the matter and what fraction of the absorbed radiation is reemitted by the x-ray heated matter.

In recent years radiative hating has been investigated in numerous experiments. The propagation of a radiative heat wave in a high-Z gold foil has been observed by Sigel *et al.* [17,18] for temperatures up to 240 eV. Radiative burnthrough in thin foils consisting of the medium-Z element germanium was studied by White *et al.* [19]. Investigations with low-Z material were limited to modest temperatures below 100 eV corresponding to x-ray fluxes lower than 10^{13} W/cm^2. Radiative burnthrough has been observed in 0.8-μm-thick Be foils and 1-μm-thick carbon plastic foils [20,21]. A direct measurement of the temperature by absorption spectroscopy in radiatively heated doped plastic foils has been performed by several researchers [22–24]. The dynamics of an expanding radiatively heated plastic foil has been studied by Edwards *et al.* [25]. An attempt [26] to measure the frequency integrated reemission from a radiatively heated wall of varying Z showed an increase of the reemission with Z.

Recently a joint experiment of the Max-Planck-Institut für Quantenoptik (MPQ) and the Institute of Laser Engineering (ILE), Osaka University, has been performed in

*Permanent address: KFKI–Research Institute for Particle and Nuclear Physics, H-1525 Budapest, POB 49, Hungary.

†Present address: Department of Micro System Engineering, Nagoya University, Furo-cho, Chikusa-ku, Nagoya, Aichi 464-01, Japan.

which radiative heating of low-Z plastic foils has been studied at temperatures ranging from 100 to 180 eV, which are higher than those of the previous studies. The high-temperature thermal x rays were generated by focusing the output energy of the ILE Gekko XII laser (4 kJ at a pulse duration of 0.8 ns and a wavelength of 350 nm) into gold cavities. Radiative burnthrough of CH plastic foils was observed up to a thickness of 15 μm (corresponding to a mass density of 1.6 mg/cm^2). These results allowed us to determine the x-ray ablation rate as a function of the temperature. In a few shots we also studied radiative burnthrough in CF_2 [polytetrafluoroethylene (PTFE)] foils. The burnthrough studies were completed by the measurement of the reemission (the self-emission, also called the albedo) from the heated layer. A good discrimination against the emission from the high-Z gold plasma was important for the measurement of the weak reemission of the low-Z material. Some of these results have been published recently by us in Ref. [27]. It is noted that the experiments with Gekko XII were preceded by test experiments [28] performed with the MPQ laser Asterix IV of lower energies and of a shorter pulse duration at temperatures around 100 eV.

In this paper we describe the results of the joint MPQ-ILE experiment in detail. The experimental setup and the results are presented in Secs. II and III, respectively. A discussion follows in Sec. IV by comparing the experimental results with numerical radiation hydrodynamic calculations performed with the MULTI computer code. A summary is given in Sec. V.

II. EXPERIMENTAL ARRANGEMENT

The experiments were performed with the Gekko XII laser of the ILE of the University of Osaka. The laser has ten beams, each delivering 500 J energy with a pulse width of 0.8 ns [full width at half maximum (FWHM)] at a wavelength of 0.35 μm. The *Hohlraum* targets were fabricated from gold. We used two different types (Fig. 1). The target shown in Fig. 1(a) (denoted in the following as type TC) consists of two outer converter parts and a central cylindrical part 1 mm in length and 1 mm in diameter. Two bundles, each consisting of four Gekko XII beams, hit the converter part where the laser is converted into x rays. The spectroscopic investigation took place in the indirectly heated central cylindrical portion of the cavity, which allowed both x-ray reemission and x-ray burnthrough experiments. For that purpose the target had two lateral opposite diagnostic holes with a diameter of 400 μm marked by 1 and 2 in Fig. 1(a). In the case of reemission experiments the reemitter foil was glued onto hole 1, as shown in Fig. 1(a). The foil was chosen to be thick enough (≥ 6 mg/cm^2) to absorb all the heating x rays. Hole 2 served as a diagnostic hole for the reemitted radiation. For studying the radiative burnthrough of the plastic foils, hole 1 was closed by a gold emitter and the absorber foil was glued onto diagnostic hole 2. Due to the strong heating by intense x rays from the cavity, a thin enough foil becomes transparent, resulting in a characteristic burnthrough spectrum. To avoid edge effects from the diagnostic hole, a diaphragm of a smaller

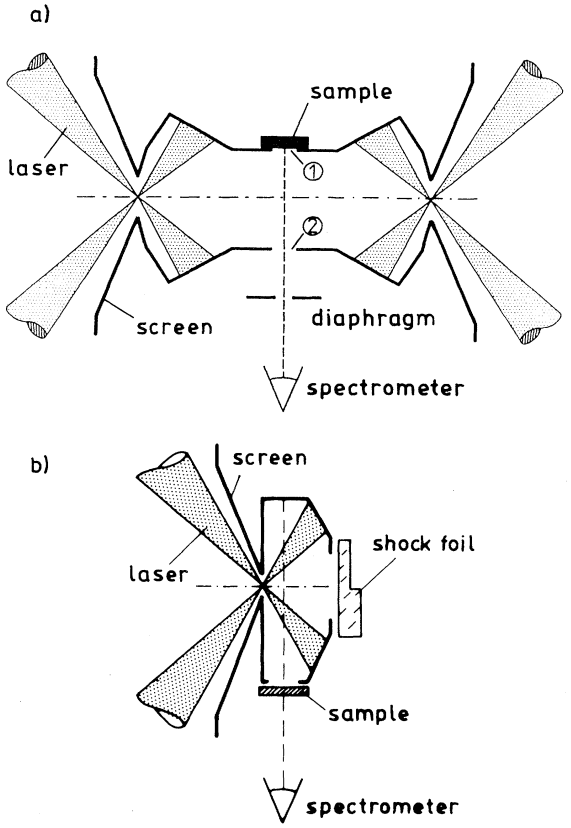

FIG. 1. Experimental arrangement for (a) clean cavities and (b) D-shaped cavities.

diameter of 200 μm was positioned at a distance of 0.7 mm from the diagnostic hole both for absorption and emission experiments.

The shape of the TC-type target has been chosen to ensure that neither direct nor reflected laser radiation could illuminate the investigated sample. Thus the sample was only heated by thermal x rays emitted from the gold wall of the cavity. Moreover, the large distance between the converter part of the central cylinder avoided a rapid filling of the central cylinder by hot plasma generated in the direct laser spots. This is of particular importance for the measurement of the reemission from the sample, which must not be disturbed by the emission from gold plasma filling the central cavity.

In addition to the TC-type target, D-shaped cavities have also been used [Fig. 1(b)] (denoted TD in the following). They were illuminated from one side by a bunch of four or five Gekko XII laser beams with a maximum total energy of 2.5 kJ. Cavities of three different sizes have been used with inner surfaces equivalent to hollow spheres of 1, 2, and 3 mm (denoted in the following by TD1, TD2, and TD3, respectively). Because of the fast plasma filling, the D-shaped cavities are not appropriate for reemission measurements and were used only for burnthrough experiments, which, however, could be extended with this type of target to higher temperatures compared to the TC target. The burnthrough sample

foils were glued onto a lateral diagnostic hole, whereas the rear hole on the symmetry axis served for other investigations that have been performed in parallel to the experiment described here, namely, of the study of a radiatively driven shock wave [13] and of a radiatively heated low-density foam sample [29]. Figure 1(b) shows a stepped witness plate on the rear hole, which allowed us to measure the shock velocity.

The reemitted or transmitted radiation was measured in the extreme ultraviolet spectral range 250 eV $\leq h\nu \leq$ 1 keV by a spectrometer equipped with a 5000 lines/mm transmission grating and an x-ray streak camera (XRSC) [30] as a detector. The spectral and the temporal resolution were 0.07 nm and 30 ps, respectively. We prepared a carbon-free cathode for the XRSC in order to investigate carbon x-ray spectra. It consisted of a 1100-Å-thick CsI layer evaporated on a 740-Å-thick aluminum substrate. Because it was not easy to fabricate such a cathode of good homogeneous quality, we selected from a larger number a sample as homogeneous as possible. The employed photocathode is nearly as sensitive as the most often used CsI evaporated on carbon, but its spectral response does not contain the carbon K edge within the range of investigation. Its spectral response has been obtained by calculation, in the same way as described by Tsakiris [30] for the standard CsI cathode on carbon. We note that the spectral response is required for the analysis of the XRSC reemission spectra. In contrast, the transmission is independent of the spectral response of the spectrometer because it is obtained by normalizing the spectrum observed through an absorber foil to the spectrum emitted by the gold wall seen without absorber foil.

In addition to the 5000 lines/mm spectrometer, the radiation emitted from the inner gold wall of the cavity was monitored in each shot through another diagnostic hole (not shown in Fig. 1) by a second XRSC combined with a 1000-lines/mm transmission grating spectrometer and by a time-integrated pinhole grating spectrometer with absolutely calibrated Ilford Q plates [31] as detector. In order to reduce the soft-x-ray background radiation, pinhole grating spectra filtered by 7 μm of Be were recorded in the spectral range above 500 eV. The unfiltered and the filtered time-integrated spectra together with the x-ray pulse duration measured by the XRSC allowed us to measure a reliable brightness temperature of the gold wall. This procedure has been described previously [6].

Care was taken to shield the diagnostic holes from each other. The special screens seen in Fig. 1 were applied to shield the external wall of the cavity from the illumination by the unfocused first and second harmonic radiations of the Gekko XII laser, which might have created plasma on the external surface of the cavities.

The samples we used were CH plastic foils, namely, parylene (C_8H_8, $\rho=1.05$ g/cm^3) or polypropylene (nCH$_2$, $\rho=0.9$ g/cm^3) and in a few shots PTFE (Teflon) foils (CF_2, $\rho=2.2$ g/cm^3). As the mass densities are different, we shall use mass per area units to characterize the sample thickness in the following.

III. EXPERIMENTAL RESULTS

A. Radiation temperatures

As described in more detail in the model of Sigel [32], the total radiation flux (S_c) that is incident on a wall element is composed of the source flux (S_s) emitted by the direct laser spots and the flux (S_i) emitted from other wall elements, i.e., $S_c=S_s+S_i$. A wall element irradiated then by the cavity flux S_c absorbs some fraction of it (S_a) and reemits another fraction (S_r), resulting in the balance

$$S_c=S_a+S_r \ . \tag{1}$$

The ratio $r=S_r/S_c$ is the reemission (or albedo) of the wall. It is expected to be large (close to unity) for a high-Z wall like a gold wall, i.e., for gold it is $S_r \approx S_c$. In contrast, r is small for low-Z matter, where $S_a \approx S_c$.

By using Boltzmann's law we relate S_c and S_r to temperatures: $S_c=\sigma T_c^4$ and $S_r=\sigma T_r^4$. T_r is the *brightness temperature* of a radiating wall element. T_c is an effective temperature characterizing the total flux S_c. We use this definition of T_c, although S_c may deviate considerably from an ideal isotropic Planckian flux, for example, due to the presence of the hot, direct laser spots or the presence of holes in the cavity. Because S_c is responsible for driving the heat wave into the wall, we denote T_c in the following as *drive temperature*. T_r and T_c are related by the reemission: $T_r/T_c=r^{1/4}$. For high-Z wall material with r close to one, T_r is close to T_c. We used two

TABLE I. Measured temperatures for different cavities at different laser energies E_L. T_r is the spectroscopically measured gold wall brightness temperature and T_c is the temperature derived from the shock speed v_s.

Cavity type	E_L (kJ)	T_r (eV) (spectroscopy)	T_c (eV) (shock wave)	v_s (10^6 cm/s)
TC	3.88±0.06	121±15		
TD1	2.06±0.04	152±8	150±5	3.28±0.13
TD1	2.53±0.05	164±10		
TD2	2.08±0.05	108±6	123±4	2.38±0.10
TD2	2.39±0.10	123±6		
TD3	2.24±0.05	92±5	97.5±3.0	1.61±0.07
TD3	2.63±0.05	95±5		

methods to measure temperatures: We performed a spectroscopic measurement of the radiation reemitted by a gold wall element resulting in the gold brightness temperature and we derived the drive temperature from the speed of the radiatively driven shock in aluminum.

1. Spectroscopic method

To get the gold brightness temperature (according to the procedure of Nishimura *et al.* [6]) we integrated the gold wall emission spectra measured absolutely by the time-integrated pinhole transmission grating spectrometer in the spectral range from 90 eV to 2 keV. Furthermore, we assume that the radiating gold wall layer is optically thick, i.e., that the angular distribution of the emitted radiation follows Lambert's law. (Note that we did not measure the angular distribution, but only the emission along the normal of the gold wall element.) The actual time duration of the reemitted pulse recorded by the XRSC was taken into account. We measured the shortest pulses (530±30 ps) for the smallest cavity TD1 and longer pulses up to 900 ps for the larger D-shaped cavities TD2 and TD3. With the TC cavity the typical durations were 500–600 ps. A similar dependence on the cavity size has been observed and discussed previously [6].

The spectroscopically obtained gold wall temperatures are presented in Table I. The errors given there are consequences of shot to shot variations and of the absolute calibration accuracy. As found previously with spherical cavities, the temperature scales with the averaged incident laser flux $\bar{S}_L$, which is obtained by dividing the laser energy E_L by the inner cavity area A_c and the laser pulse duration τ_L [$\bar{S}_L = E_L/(A_c\tau_L)$]. Figure 2 shows for the nonspherical cavities of this experiment

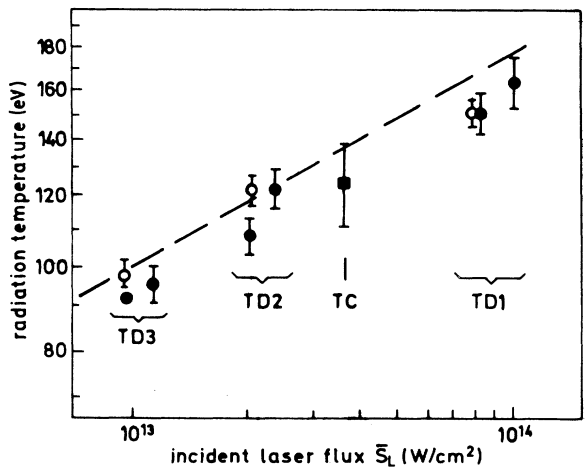

FIG. 2. Temperature versus the mean laser intensity $\bar{S}_L$. The measured points are obtained from different cavity types TC, TD1, TD2, and TD3. Full symbols, spectroscopically measured brightness temperature of the gold wall; open dots, drive temperatures derived from the shock speed in aluminum, dashed curve, $T=(\bar{S}_L/\sigma)^{1/4}$ with σ the Stefan-Boltzmann constant.

how the temperature depends on $\bar{S}_L$. The measured brightness temperatures are somewhat below the dashed line on which the temperature is given by $\bar{S}_L=\sigma T^4$. In contrast, the brightness temperature found previously with spherical cavities (compare Fig. 7 of Ref. [6]) were slightly above this line, i.e., somewhat higher than for the nonspherical cavities of this experiment.

Our brightness temperature measurement is in good agreement with recent results in two-dimensional simulations for the nonspherical cavities used by us [33]. These calculations have been carried out for the TD2 cavity irradiated by a laser energy of 2 kJ. For the lateral wall element that is used for the spectroscopic measurement, a maximum brightness temperature of 113 eV was predicted. It is noted that the calculated brightness temperature differed slightly on different wall elements. For example, for a rear axial wall element (where the shock speed was measured; see Sec. III A 2) 105 eV was obtained, which is 8 eV lower than the value for a lateral wall element.

An example of the reemitted gold spectrum is exhibited in Fig. 7 for the TC cavity. The spectra of the TD2 cavity with about the same temperature is quite similar to this spectrum, whereas the spectra of TD1 and TD3 are shifted somewhat to shorter and longer wavelengths, respectively.

2. Shock speed method

Recently it has been demonstrated by Kauffman *et al.* [7] that the temperature can be derived from the velocity of the radiatively driven shock propagating into aluminum. Aluminum is an appropriate material for this purpose because its equation of state is well known [34]. Since the shock speed has been measured in the present experiment [13], we have applied this method too.

The speed v_s of the shock propagating into the aluminum shock target is determined by the total incident flux S_c. Some fraction of it ($S_a/S_c \approx 70\%$ for aluminum under the conditions here) is absorbed by the wall and an ablative heat wave related with an ablation pressure is driven into the aluminum wall. The shock speed v_s is then related to the pressure via the Hugoniot relation. The exact dependence of T_c on v_s may be obtained by numerical hydrodynamic code simulations. For a pulsed cavity flux S_c of 3 ns in duration, Kauffman *et al.* [7] found the result

$$T_c = 0.0126 v_s^{0.63} , \tag{2}$$

where T_c is in units of eV and v_s in units of cm/s.

By means of our MULTI hydrodynamic code simulations, which are described in more detail in Sec. IV, we have reproduced Eq. (2) for a 3-ns drive pulse in the temperature range 100–300 eV (with the relative deviation $\Delta T_c/T_c$ not exceeding 3%). In these simulations we assumed an isotropic Planckian flux S_c incident on the aluminum shock target. The shock speed depends slightly on the x-ray pulse duration. For the shorter pulse duration of our experiments we find the result

$$T_c = 0.0184 v_s^{0.60} . \tag{3}$$

We have applied Eq. (3) to determine T_c. The measured shock speeds are taken from [35] and listed in Table I along with the calculated drive temperature values T_c. The obtained drive temperatures T_c are also plotted in Fig. 2 (open dots). The errors given for T_c are due to the error of the measured shock speed ($\Delta v_s/v_s = \pm 4\%$).

The drive temperatures obtained from the shock speed are close to the spectroscopic temperature values T_r with the trend to be slightly larger. This behavior is in accordance with the large reemission (close to one) expected for the gold wall cavity [$T_r/T_c = (S_r/S_c)^{1/4} = (r_{Au})^{1/4}$]. In principle, the gold reemission $r_{Au} = S_r/S_c$ can be determined from the measured temperatures T_r and T_c. However, this requires a high measuring accuracy, which (in particular for T_r) was not available in our experiment. Also, in the present experiment we measured the shock speed and the brightness temperatures at different wall elements [compare Fig. 1(b)], which may have slightly different temperatures. As noted above, the two-dimensional calculations of Ramis and Meyer-ter-Vehn [33] predicted for the rear axial wall element (where we measured the shock speed) a lower temperature than for the lateral wall element of the spectroscopic measurement.

B. Burnthrough measurements

1. CH foils

Figure 3 shows streaked x-ray transmission spectra for CH absorber foils of two different thicknesses observed with the TD cavity. We first discuss the case of the thinner foil with a thickness of 0.52 mg/cm^2 [Fig. 3(a)]. The radiative burnthrough starts at the carbon K edge, which is becoming less and less steep than that of cold carbon at $\lambda = 44$ Å. Also, in the beginning the K edge is slightly shifted to longer wavelengths. With subsequent heating it moves towards shorter wavelengths and the foil starts to become transparent above the K edge ($\lambda < 44$ Å), showing an absorption spectrum characteristic for ionized carbon with the characteristic absorption lines of heliumlike and hydrogenlike carbon.

In a thicker foil [0.79 mg/cm^2; Fig. 3(b)] the burnthrough is slower. The early stage of the burnthrough, i.e., the smoothing and initial redshift of the cold carbon K edge, extends here over a longer period and it takes quite a long time until transmission between the heliumlike He-α and He-β lines sets in. No transmission is observed in the region of the hydrogenlike lines. At the shortest wavelengths (10 Å $< \lambda <$ 20 Å) transmission is seen from the beginning due to the fact that the cold foil already is partially transparent here [similarly to Fig. 3(a)].

The transmission spectra that were obtained by normalizing the streaks of Fig. 3 to the emission from the gold wall [see Fig. 6(a)] are plotted in Fig. 4. For comparison we have also plotted the transmission of the cold foil, which was calculated from the data of Henke *et al.* [36]. The spectrum of the thinner foil [Fig. 4(a)] was taken 0.2 ns after the peak of the x-ray emission from the gold wall [Fig. 6(a)]. [Throughout this paper the given times refer to the maximum of the reemitted gold signal that was monitored in each shot. We set $t = 0$ in this maximum (compare Figs. 6 and 8).] We observe clearly the strong absorption lines of the heliumlike $1s^2$-$1s2p$ (He-α) and $1s^2$-$1s3p$ (He-β) and of the hydrogenlike $1s$-$2p$ (Ly-α) and $1s$-$3p$ (Ly-β) transitions. Transmission windows appear between these absorption lines. In the following we denote the transmission window between the He-α and He-β lines as W1 and between the Ly-α and Ly-β lines as W2. The inset illustrates how these two transmission windows open with time. The burnthrough in the W2 window follows the burnthrough in the W1 window with a delay of 0.2 ns.

The weaker transmission of the thicker foil (0.79 mg/cm^2) is illustrated in Fig. 4(b). Although this transmission spectrum was taken later, at $t = 0.6$ ns, the transmission remains much lower than in Fig. 4(a). In the He-like W1 window the maximum transmission of 40% was reached in a spectral range that is narrower than in Fig. 4(a). The H-like W2 feature is still in the noise level. The inset in Fig. 4(b) shows the temporal in-

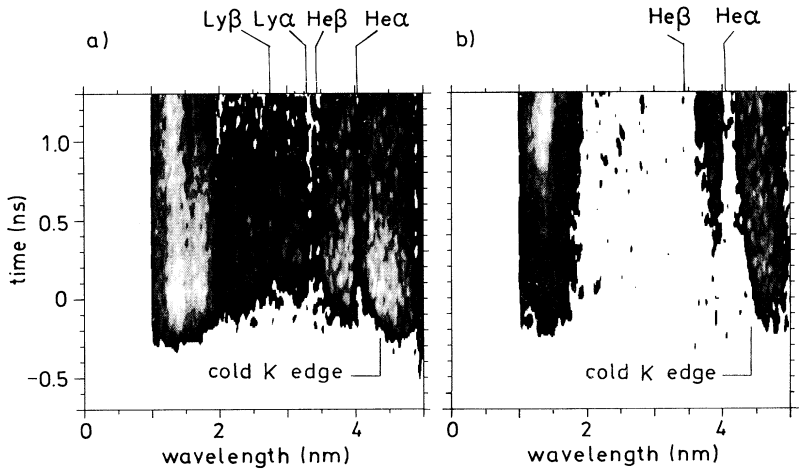

FIG. 3. Time-dependent absorption spectra of (a) 0.52-mg/cm^2 and (b) 0.79-mg/cm^2 CH foils measured with the TC cavity. The data are cut at $\lambda < 10$ Å, the region perturbed by zeroth-order contributions from the transmission grating spectrometer.

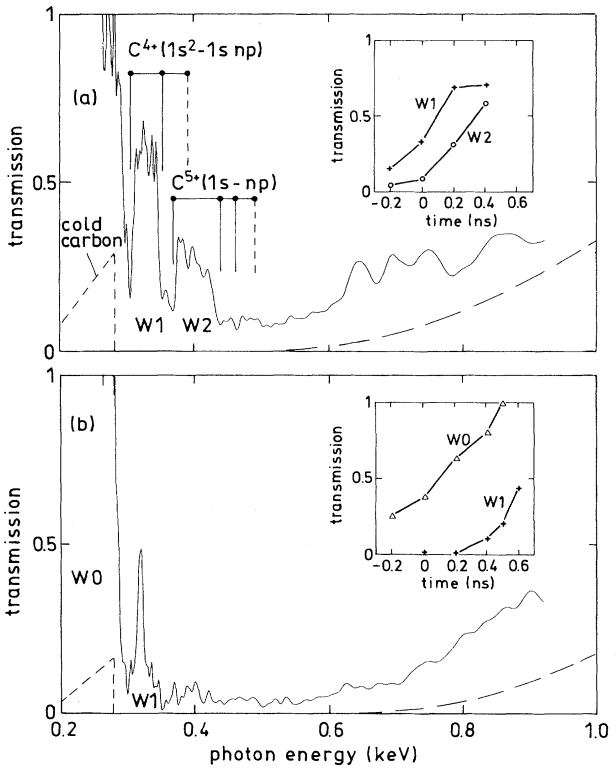

FIG. 4. Transmission spectra (normalized to the gold wall emission) of (a) 0.52 mg/cm^2 of parylene at $t=200$ ps and (b) 0.79 mg/cm^2 of polypropylene at $t=600$ ps, averaged over 200 ps. The inserts show the time dependence of the burnthrough in the transmission window (a) between the $1s^2$-$1s2p$ and $1s^2$-$1s3p$ transitions (W1) and between the $1s$-$2p$ and $1s$-$3p$ transitions (W2) and (b) between the $1s^2$-$1s2p$ and $1s^2$-$1s3p$ transitions (W1) and below the K edge (W0).

crease of the He-like W1 window together with the increase of the transmission below the K edge (W0) from the initial cold-matter value. Note that for the thinner foil [Fig. 4(a)] the transmission for W0 was high from the beginning.

The burnthrough behavior of the CH foils heated by the TD2 cavity was the same as that observed with the TC cavities. This is expected because these cavities had about the same temperature (see Table I). With the hotter TD1 cavities parylene burned through at thicknesses up to 15 μm (corresponding to 1.58 mg/cm^2). A transmission spectrum of a 10-μm (1.05-mg/cm^2) parylene foil is shown in Fig. 5(a) at $t=600$ ps. (It will be compared in the next section with the transmission spectrum of a CF_2 foil.) The spectrum shows transmission up to 1 keV photon energy where the transmission exceeds considerably the cold carbon transmission (dashed line) due to the high ionization of carbon.

Our burnthrough results are summarized in Table II. It shows, for the different cavities at different laser energies, the time interval Δt, which is needed by the heat wave to propagate through the foil. Δt is obtained from $\Delta t=t_1-t_0$, where t_1 is the time when the transmission in the characteristic He-like W1 transmission reaches 50%. As will be shown in Sec. IV, t_1 indicates the arrival of the radiative heat wave at the rear side of the burnthrough foil. For t_0 we took the time when the reemission signal from the gold wall starts. Typically, this occurs 0.4–0.5 ns before the maximum of the reemission signal; compare the time-dependent reemission pulses presented in Sec. III C, Figs. 6 and 8. We assume that t_0 corresponds to the time when the radiative heat wave starts at the front side of the foil. From the foil thickness m and the time interval Δt we calculated the characteristic velocity of the radiative heat wave propagating through the foil: $\dot{m}=m/\Delta t$. Because the foil expands at the same time, $\dot{m}$ also corresponds to the mass ablation rate. The values obtained for $\dot{m}$ are listed in Table II. They will be discussed further in Sec. IV.

We finally note that the burnthrough behavior seen here is characteristic of low-Z matter, when it is ionized to heliumlike and hydrogenlike species. It has also been previously observed with Be at lower temperatures [21,37].

2. CF_2 foils

In addition to CH foils we also measured burnthrough spectra of CF_2 foils. Figure 5 compares the transmission spectra of a 1.05-mg/cm^2-thick parylene foil (C_8H_8) [Fig. 5(a)] with a 0.88-mg/cm^2-thick PTFE foil [Fig. 5(b)]. Because of the high fluorine fraction (76% of the total mass) the CF_2 burnthrough spectrum is dominated by fluorine, which has its cold K edge at 687 eV. The spectral struc-

TABLE II. Mass ablation rates according to the measurement and simulation for different cavity types. E_L is the laser energy of the individual shot and Δt is the duration for heat wave propagation through the foil. The error of the measured mass ablation rate is mainly given by the uncertainty in the measurement of Δt.

Cavity type	E_L (kJ)	Mass (mg/cm^2)	Δt (ns)	$\dot{m}$ (g cm^{-2} s^{-1}) Measurement	Simulation
TC	3.94	0.79	1.05±0.10	$(7.5\pm0.8)\times10^5$	1.05×10^6
TC	3.89	0.52	0.55±0.10	$(9.5\pm1.8)\times10^5$	1.1×10^6
TD1	2.52	1.05	0.65±0.10	$(1.60\pm0.25)\times10^6$	2.2×10^6
TD1	2.07	1.58	1.15±0.10	$(1.30\pm0.12)\times10^6$	1.8×10^6
TD2	2.48	0.52	0.75±0.10	$(7.0\pm1.0)\times10^5$	1.0×10^6
TD3	2.03	0.35	0.85±0.10	$(4.1\pm0.5)\times10^5$	5.4×10^5

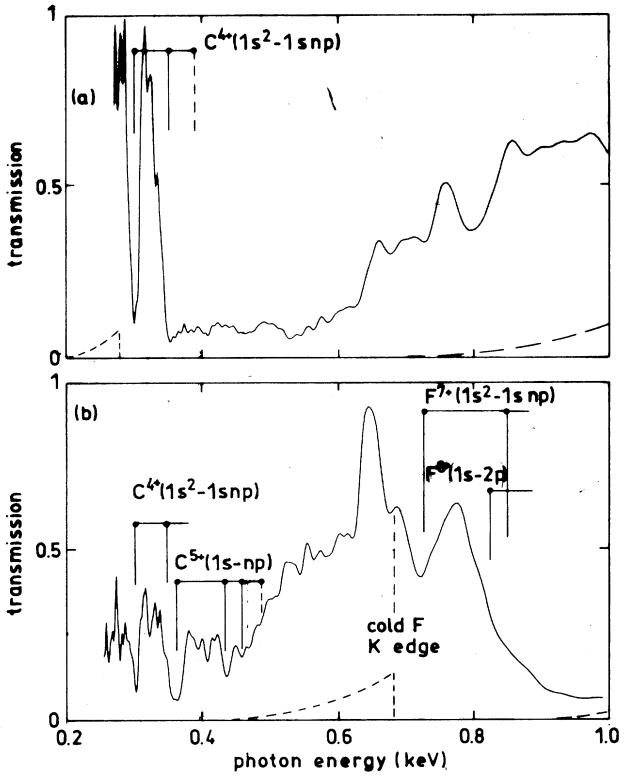

FIG. 5. Transmission spectra measured with the TD1 cavity. (a) 1.05-mg/cm^2-thick CH foil at $t=600$ ps; (b) 0.88-mg/cm^2-thick CF_2 foil at $t=300$. The spectra are averaged over 200 ps.

ture seen in Fig. 5(b) around the fluorine K edge corresponds to that seen with carbon around the C K edge. (The fluorine structure appears to be smoother than that of carbon because of the lower resolution at higher photon energies: $\Delta E \propto \Delta\lambda/\lambda^2$ with $\Delta\lambda=0.07$ nm, which is constant in the whole spectral range.) Due to the ionization of fluorine the transmission below the fluorine K edge is strongly increased up to nearly 100%. Above the fluorine K edge the fluorine He-α absorption line at 738 eV is seen, along with the transmission window between the He-like fluorine lines (corresponding to the carbon W1 window), which shows here 60% transmission. At higher photon energies up to 1 keV the transmission decreases to about 5% because of the efficient absorption by the fluorine K-shell electrons in this spectral range. In contrast, the carbon spectrum of the CH foil [Fig. 5(a)] transmits about 50% in this range. It is noted that also the temporal development of the fluorine structure corresponds to that of carbon: First the region below the fluorine K edge becomes transparent and then transmission sets in the fluorine W1 window. From this opening of the fluorine W1 window one can guess the mass ablation rate in the CF_2 foil, similarly to what has been done in Sec. III A for the CH foils. We find for the time needed by the heat wave to propagate through the CF_2 foil $\Delta t=0.65$ ns, resulting in $\dot{m}=1.4\times10^6$ g cm^{-2} s^{-1}, which is close to the value found for CH foils heated by the TD1 cavity (Table II).

Besides the fluorine structure Fig. 5(b) also shows the characteristic carbon structure around the C K edge. However, as compared to Fig. 5(a), the transmission is smaller because it is influenced by photoionization of the fluorine L-shell electrons. This means that there is still a considerable amount of fluorine ions present with bound L-shell electrons at the temperatures reached in the CF_2 foil causing absorption.

C. Reemission of CH foils

Figure 6 presents x-ray streak camera images of the reemission of a gold and of a carbon element heated in the TC target. Figure 6 was obtained after deconvolution with the sensitivity of the XRSC photocathode. It is noted that for recording the reemission from carbon, which is considerably less than the reemission from gold, the streak camera was switched to a higher gain; thus the isointensity contours in Figs. 6(a) and 6(b) correspond to different intensities. A quantitative comparison of the gold and the carbon spectrum is shown in Fig. 7. These spectra are time integrated from $t=-0.35$ until 0.25 ns. In a few spectral regions there is an uncertainty due to problems with the photocathode of the XRSC. In these regions the spectra are dashed in Fig. 7. Around 480 eV the cathode had a spatial inhomogeneity. The structures seen at 0.65 keV is probably caused by difficulties in the deconvolution of the spectral response of the XRSC photocathode. (Both Cs and I have their M edges here, which could not be completely smoothed out by the deconvolution.) We note that these uncertainties are not relevant for the transmission spectra because they cancel due to the normalization.

For a correct measurement of the smaller carbon reemission it is necessary that contributions caused by the emission from the gold plasma expanding from the cavity wall into the line of sight of the spectrometer are small. To check this we compared the carbon reemission with the signal obtained by looking through the two holes 1 and 2 when they were open. In this case only the radiation of the gold plasma filling the cavity could be seen. It was found that the radiation of the plasma filling is practically negligible within a duration of 0.6 ns until $t=+0.25$ ns. This is demonstrated by the background spectrum plotted in Fig. 7, which is weak compared to the carbon spectrum, in particular, in the spectral range 0.3–0.6 keV, where the carbon emission predominantly occurs. Moreover, with the carbon reemitter the background from the gold filling seemed to be suppressed, as judged from the XRSC images. The cause may be that the fully stripped, light carbon ions fill up the cavity faster, preventing its filling with the partially stripped, heavy gold ions.

The measured gold reemission exceeds, in the whole spectral range, the carbon reemission (Fig. 7). It has two peaks at approximately 0.3 and approximately 0.5 keV with a minimum at approximately 0.37 keV, where the intense carbon lines appear. This structure is a general feature of gold x-ray spectra in the temperature range of this experiment [3]. It is also visible in calculated gold opacities [38]. The peaks of the gold spectrum are caused

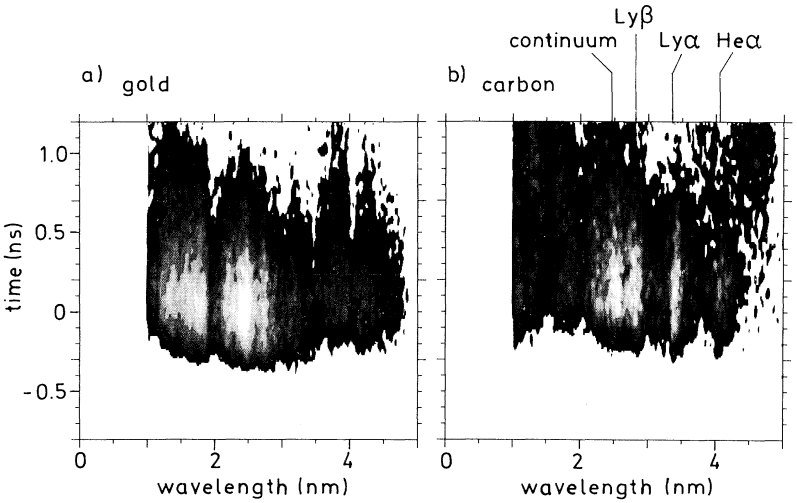

FIG. 6. Time-dependent reemission spectra measured with the TC cavity. Emission from (a) a gold wall element and (b) a carbon wall element. In (b) the XRSC sensitivity is higher by a factor 3.

by transitions between the $4d$ and $4f$ subshells and by transitions between the $n=4$ and 5 main shells as indicated in Fig. 7. The observed carbon spectrum is dominated by broad lines (He-α, Ly-α, and Ly-β) and a strong contribution from the free-bound (FB) continuum. It is characteristic to the emission of a thick hot carbon layer. Because of its increasing temperature and thickness with time the spectrum shows a time dependence. The detailed analysis of the streak spectrum [Fig. 6(b)] shows that at the beginning ($t<-0.35$ ns) the He-α and Ly-α lines have the same height and the He-β line is still separated from the Ly-α line. Later on the Ly-α line becomes dominant and the He-β line appears only as a shoulder of the Ly-α line. The FB continuum is small in the beginning and increases with time due to the increasing heated layer thickness.

A comparison of the frequency-integrated reemitted flux from a gold and a carbon wall is shown in Fig. 8, where it is plotted versus time. The maximum of the carbon reemission appears somewhat later than that of gold. The ratio of the reemitted flux of carbon and gold increases with time from 10% to 30%. The time-averaged total reemission of carbon is (23±5)% of the gold reemission. The carbon reemission depends on the cavity flux. In a shot with a significantly lower laser energy and consequently lower wall temperature, i.e., 114 eV as compared with 127 eV, the observed carbon reemission was only (14±3)% of the gold reemission. The error of the carbon to gold reemission ratio is due to the fact that the gold and carbon reemission was measured in different shots.

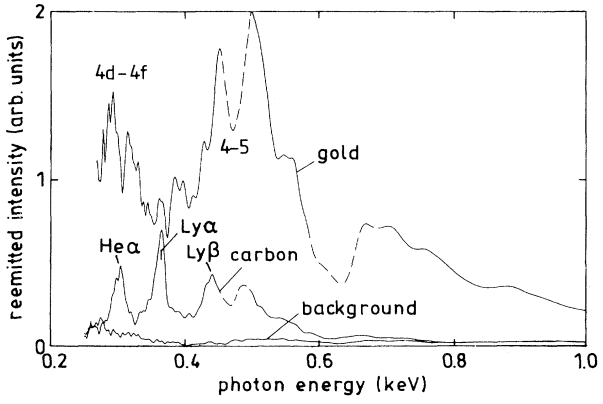

FIG. 7. Reemission spectra of Au and CH as compared by the signal obtained by looking through the cavity. The spectra are averaged from −0.35 to +0.25 ns, i.e., for the time interval before strong plasma filling. The dashed section of the spectra indicates an uncertainty of the measurement (see the text).

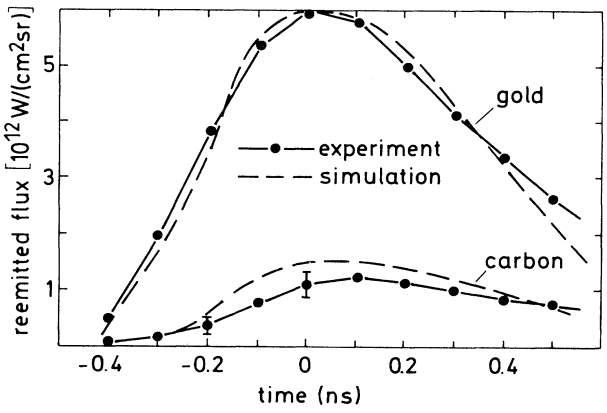

FIG. 8. Time dependence of x-ray reemission of gold and carbon heated by the TC cavity integrated within the spectral range of 1–5 nm. The experimental results (solid lines) are compared with simulations (dashed lines). The error bars on the experimental carbon data points characterize the accuracy of the ratio of the carbon and the gold reemission. There may be an additional error in the absolute scale of the ordinate, which was obtained from the time-integrated measurement on calibrated x-ray film.

IV. COMPARISON WITH HYDROCODE SIMULATIONS

A. Carbon opacities

We have performed numerical simulations of the experimental results with the one-dimensional MULTI hydrodynamic computer code [39], which describes the radiation transport by a multigroup diffusion approximation for which the radiative opacities of the material are needed. Because of the high density of the heated samples, we assume that the matter is in a state close to local thermal equilibrium (LTE), as is discussed in more detail in the Appendix. We calculated LTE opacities by means of the SNOP code, which is well documented [40]. An example of the spectral dependence of the opacity of hot carbon is shown in Fig. 9. The temperature ($T=100$ eV) and density ($\rho=0.1$ g/cm^3) chosen here are typical for the radiatively heated carbon foils of this experiment; see below. For comparison, we plotted in Fig. 9 the opacity of cold solid carbon too [36]. The mean ionization calculated for the hot carbon is $\bar{Z}=5.435$. Thus the dominant absorption lines are due to heliumlike and hydrogenlike carbon ions. In these lines the hot opacity exceeds the cold opacity, whereas between the lines the opacity drops considerably below the cold opacity, resulting in the characteristic transmission windows (W1 and W2) observed experimentally. The level to that the opacity drops in these transmission windows mainly depends on the line broadening for which electron collisional broadening [41] is the dominant mechanism for the conditions here. The region below the carbon edge (W0) is determined mainly by bound-free absorption.

We note that the SNOP code uses a number of simplifying assumptions [40]. For example, only the principal quantum number is implemented, i.e., l-splitting (l=orbital quantum number) is neglected. However, we emphasize that for the low-Z elements in the temperature and density range considered here, the SNOP code yields, in spite of these approximations, reasonable values. We would like to demonstrate this by a comparison with a much more sophisticated code, namely, the OPAL code [42,43]. There are no large deviations in the results from both codes. As shown in Table III, the values for the mean ionization as well as for the Rosseland and Planck mean opacities found by OPAL are close to the values of SNOP. The frequency-dependent opacities are in good agreement too (Fig. 9). There are some differences in the transition of the hydrogenlike line series to the continuum. The continuum limit is in both calculations somewhat above the Ly-β line. However, in contrast to OPAL, SNOP does not consider broadening of the continuum edge, for which reason a sharp step appears in the SNOP result. Another difference (by a factor of about 2) is present in the bound-free absorption in the range below the carbon edge.

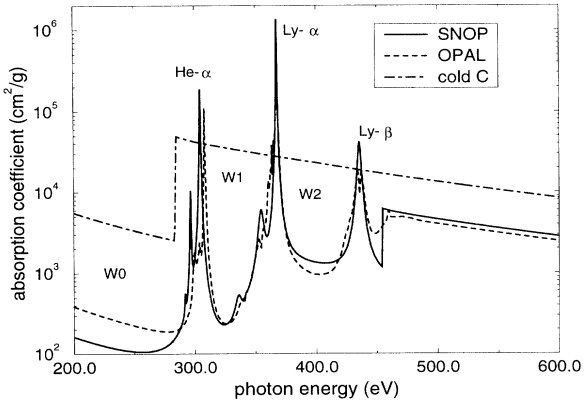

FIG. 9. Calculated carbon opacity at $T=100$ eV and $\rho=0.1$ g/cm^3. Solid line, result of the SNOP code; dashed line, result of the OPAL code of Rogers *et al.* [42]. In addition, the cold carbon opacity (from Henke *et al.* [36]) is plotted (dash-dotted line).

B. Simulation of a typical case

MULTI has the option to heat matter by isotropic Planckian radiation. The experimental conditions obtained with the TC cavity are close to this idealization, because the sample here is mainly irradiated by the indirectly heated inner cavity gold wall, which tends to emit isotropic radiation. Therefore we performed a detailed simulation of the TC experiment.

For the radiation transport we used 80 groups in the photon energy range up to 2 keV with a finer subdivision in the region of the prominent carbon lines (280–500 eV). The driving Planckian cavity flux was modulated in time by a time-dependent factor $\sin^2(\pi t/2\tau)$. The Planckian temperature was kept constant during the pulse, which is motivated by the observation that the spectrum reemitted by the gold wall does not change much during the pulse [compare Fig. 6(a)]. In order to model correctly the observed temporal dependence of the reemitted gold wall radiation (Fig. 8) we had to use an asymmetrical pulse with $\tau=0.3$ ns in its rising section and $\tau=0.9$ ns in its falling section (corresponding to a FWHM of 0.6 ns). With this temporal dependence and a drive temperature of 138 eV, the measured brightness temperature of 125 eV of the gold wall radiation (measured in this particular shot) and its temporal dependence was well reproduced (Fig. 8). The maximum of the driving cavity flux used in the situation is somewhat (by 0.15 ns, i.e., at $t=-0.15$ ns) before the maximum of the reemitted pulse at $t=0$.

This cavity flux was then applied to heat a carbon foil. Typical temperature and density profiles across a 0.52-mg/cm^2-thick carbon foil at different times are shown in

TABLE III. LTE values of the mean ionization $\bar{Z}$ and of the Rosseland κ_R and Planck κ_P mean opacities for a carbon plasma at $T=100$ eV and $\rho=0.1$ g/cm^3 according to the models SNOP and OPAL.

Model	$\bar{Z}$	κ_R (cm^2/g)	κ_P (cm^2/g)
SNOP	5.44	5.31×10^2	3.89×10^3
OPAL	5.34	7.83×10^2	4.88×10^3

Fig. 10. One observes a temperature wave penetrating into the carbon, which is accompanied by expansion resulting in the time-dependent density seen in Fig. 10. The heat wave has reached the rear side of the foil by the time $t=0$.

Transmission spectra (as well as reemission spectra) have been calculated by a post processor, which solves the radiation transport equation for the temperatures and densities calculated by MULTI [40]. The postprocessor has been used to increase the spectral resolution compared to the multigroup approximation of MULTI to allow us a better comparison with the measured spectra. The postprocessed spectra given in the following are smeared with the experimental spectral resolution. Figure 11 exhibits the transmission spectra obtained for the temperatures and densities at the different time steps of Fig. 10. Similar to the experiment, the spectra in Fig. 11 show the typical shape with the subsequent opening of the transmission windows W0, W1, and W2. A comparison of Figs. 10 and 11 shows that the time when the transmission in the W1 window reaches 50% corresponds to the time when the temperature at the rear side of the foil reaches 50% of its maximum value. This happens here at $t\approx 0$. We used this criterion to derive the experimental velocities of the heat wave propagation or mass ablation rate $\dot{m}$ given in Table II.

A detailed comparison of simulated and measured spectra is shown in Fig. 12. The simulated transmitted

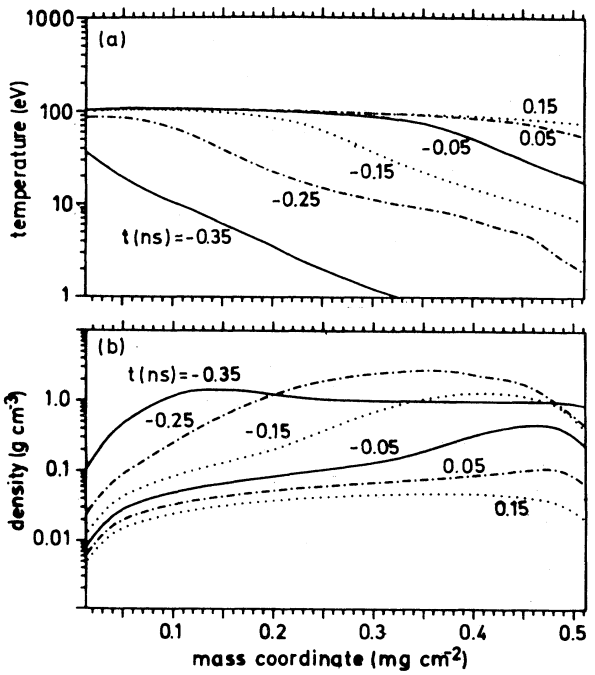

FIG. 10. Time evolution of (a) temperature and (b) density of the 0.52-mg/cm^2 CH foil as calculated by the MULTI hydrodynamic code. The foil is irradiated from the left-hand side by isotropic Planckian x rays at a temperature of 138 eV and a FWHM of 0.6 ns corresponding to the conditions of the TC cavity.

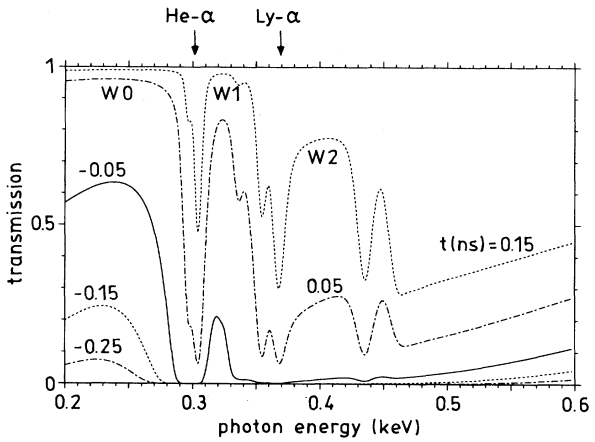

FIG. 11. Time evolution of the transmission spectra as calculated by postprocessing the hydrodynamic MULTI results of Fig. 10.

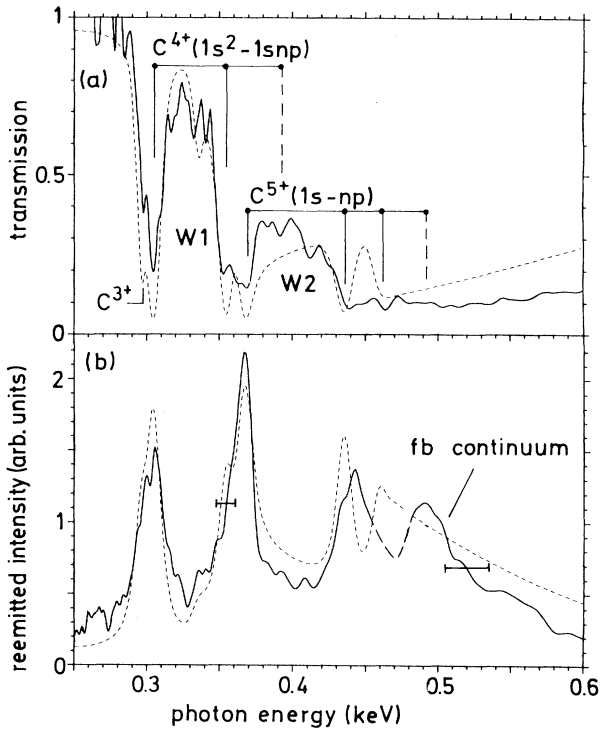

FIG. 12. Carbon transmission and reemission spectra obtained with the TC cavity. (a) Measured transmission spectrum of 0.52 mg/cm^2 of parylene at $t=200$ ps averaged over 200 ps (solid line) compared with the theoretical spectrum (dashed line) and (b) measured carbon reemission spectrum (solid line) compared with MULTI simulations (dashed line). The reemission spectrum is averaged for a 600-ps duration before an increased signal from the plasma filling sets in. An uncertainty in the measured data (compare Fig. 7) exists in the dashed section of the experimental curve. The theoretical spectra in (a) and (b) are smoothed by the experimental resolution. The measured and calculated spectra in (b) are normalized to the same area under the spectrum. In (b) the free-bound continuum is indicated.

spectrum [Fig. 12(a)] exhibits a shape similar to the measured spectrum. The radiative burnthrough of the 0.52-mg/cm^2-thick foil starts in the simulation as in the experiment at $t \approx 0$. Differences are present in the detailed temporal onset of the burnthrough, which occurred in the simulation somewhat faster than in the experiment. To achieve the agreement shown in Fig. 12(a), the calculated spectrum was taken at $t = 0.05$ ns, whereas the experimental spectrum was recorded at $t = 0.2$ ns. This means that the heat wave propagates somewhat faster in the simulation than in the experiment: the simulated value of the heat wave propagation velocity is $\dot{m} = 1.05 \times 10^6$ g/(cm^2 s) compared to the experimental value $\dot{m} = 0.95 \times 10^6$ g/(cm^2 s) (compare Table II). Some discrepancy is also present in the transition of the hydrogenlike line series to the continuum: The calculation shows still a clear Ly-β line, in contrast to the measurement. It may be attributed to the theoretical description of the absorption in this transition region, as discussed in Sec. IV A.

The reemitted spectrum [Fig. 12(b)] has been calculated for a thick sample, which does not burn through. Similarly to the measured spectrum, it shows a strong free-bound continuum together with the dominant He-α, Ly-α, and Ly-β lines, which are strongly opacity broadened in the optically thick layer. The level of the valleys between the lines [as well as the size of the transmission windows in Fig. 12(a)] is mainly determined by the overlapping line wings of the electron impact broadened lines.

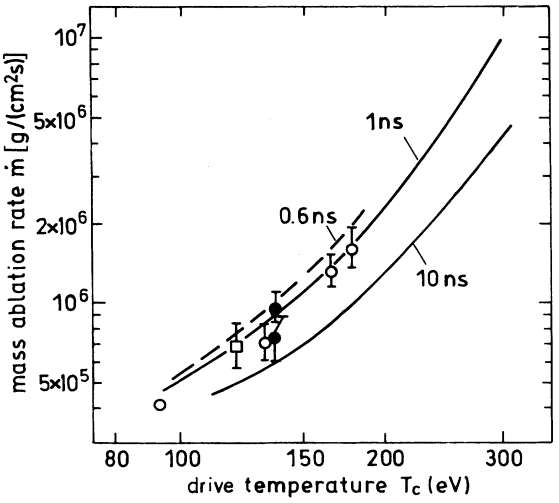

FIG. 13. Mass ablation rate $\dot{m}$ versus drive temperature. Full dots measured with Gekko XII and a TC cavity; open dots, measured with the Gekko XII laser and TD1–TD3 cavities; open square, measured with the Asterix IV laser and a spherical cavity. The drive temperatures of the experimental points are obtained from the measured gold wall brightness temperatures by correcting them with a gold reemission of 70%. The curves are simulation results. Dashed curve, calculation with an asymmetrically pulsed cavity flux with a FWHM of 0.6 ns; solid curves, calculation with symmetrical sin^2 pulse with a FWHM of 1 and 10 ns.

The simulated spectrally integrated flux (emitted along the normal of the carbon wall) was plotted in Fig. 8 (dashed line). It is slightly larger than the measured flux reemitted from carbon. The calculated time-integrated flux reemitted from carbon normalized to the corresponding value of gold is $r_C/r_{Au} = 0.26$, which is close to the experimental value of $r_C/r_{Au} = 0.23$. The gold reemission is needed to give the value of the carbon reemission normalized to the cavity flux ($r_C = S_r/S_c$). Our simulations yield a value of $r_{Au} = 0.7$ for the conditions of the TC cavity; thus we find $r_C = 0.16$. The considerably lower value of the carbon reemission compared to the gold reemission is due to the fact that the opacity of the low-Z element carbon is much less than that of the high-Z element gold. An additional reason can be attributed to our simulation result that the temperature of the gold wall is higher than that of the carbon wall (~ 130 eV compared to ~ 110 eV). This is confirmed by the experimental observation that the reemitted gold spectrum exceeds in the whole spectral range the reemitted carbon spectrum (Fig. 7). We expect that the heated gold layer is optically thick in the $4f$-$4d$ peak and in the 4-5 peak and that the heated carbon layer is optically thick in the strong Ly-α resonance line. Therefore, we guess from Fig. 7 that the gold emission has a higher Planck limit than the carbon emission. Having in mind that the height of the Planckian function scales with T^3, we can conclude from the experiment, in agreement with the simulation, that the carbon matter temperature is lower for carbon than for gold.

C. Scaling with the radiation flux

Calculations were carried out with different cavity fluxes and foil thicknesses corresponding to the experiments with different targets (Table I) in order to compare the experimental and theoretical burnthrough results in the whole temperature range of investigation. As in the previous example (Sec. IV B), an asymmetric pulse shape with a FWHM of 0.6 ns has been taken for the cavity flux, i.e., we neglected the influence of the slightly different pulse durations observed with the different cavities. The drive temperature T_c was derived from the gold brightness temperature with $r_{Au} = 0.7$. The maximum drive temperature achieved was 180 eV. The results are given in Table II to be compared with the experimental ablation rates. We find good agreement with the trend that the simulated values are somewhat higher than the measured ones. This may be attributed to deviations of the actual cavity flux from the ideal isotropic Planckian cavity flux used by the simulations. Also, the drive temperature may be overestimated due to uncertainties in the gold opacity calculated by SNOP [40], resulting in uncertainties in the gold reemission r_{Au}.

Motivated by this quite good agreement we have plotted the mass ablation rate $\dot{m}$ over a larger range of parameters (Fig. 13) at drive temperatures up to 300 eV and cavity flux pulse durations up to 10 ns. In the case of a 10-ns pulse of 300-eV temperature, which corresponds to fusion conditions [7], an ablation rate as high as $\dot{m} = 4 \times 10^6$ g cm^{-2} s^{-1} is expected, i.e, a carbon layer of

the thickness 40 mg/cm^2, corresponding to a 0.4-mm-thick layer at a density of 1 g/cm^3, should burn through. Because the ablation rate depends on the pulse duration, the exact value will depend on the detailed pulse shape.

We have also calculated with our model the reemission of carbon over an extended range of parameters. Figure 14 shows $r=S_r/S_c$ versus the pulse duration at different drive temperatures. We have plotted two experimental points here. In addition to the result obtained in this experiment with the Gekko XII laser with the TC cavity, a result obtained with the Asterix laser (200 J within 0.4 ns) and a spherical cavity [28] is plotted. We find that the reemission increases with the pulse duration τ and the cavity flux S_c. This is caused by the increase of the thickness of the heated carbon layer with τ and S_c, i.e., the carbon layer becomes more and more optically thick in the whole spectral range. In addition, with increasing τ more and more the carbon matter temperature approaches the drive temperature. We note that the detailed value of the carbon reemission is of importance for the coupling efficiency of radiation energy to the low-Z pellet in a high-Z cavity in indirect drive ICF [16]. A lower reemission may be attainable with an ablator of a smaller Z such as beryllium.

V. SUMMARY

During a joint experiment between the MPQ and the ILE we performed a detailed study of the radiative heating of low-Z plastic foils at temperatures exceeding 100 eV by using the Gekko XII laser. We find the following experimental results. (i) The radiation temperature was obtained by two methods: We measured spectroscopically the gold wall brightness temperature and we derived the temperature from the shock speed radiatively driven into aluminum. The two methods showed good agreement. (ii) For the radiatively heated low-Z plastic foil samples we measured transmission spectra at drive temperatures ranging from 100 to 180 eV. From these burnthrough spectra we derived mass ablation rates and their scaling with the cavity flux. (iii) For a clean measurement of the radiation reemitted from carbon, which on a low level, is compared to the gold reemission, it was necessary to find clean conditions free of perturbations caused by the luminosity of the gold plasma, which fills the cavity. This was achieved with a specially shaped cylindrical target. With this target having a brightness temperature of 125 eV we found that the carbon foil reemitted a fraction of 23% of the reemission from gold. This small fraction is caused by the low carbon opacity compared to gold as well as by the lower matter temperature in carbon as compared to gold.

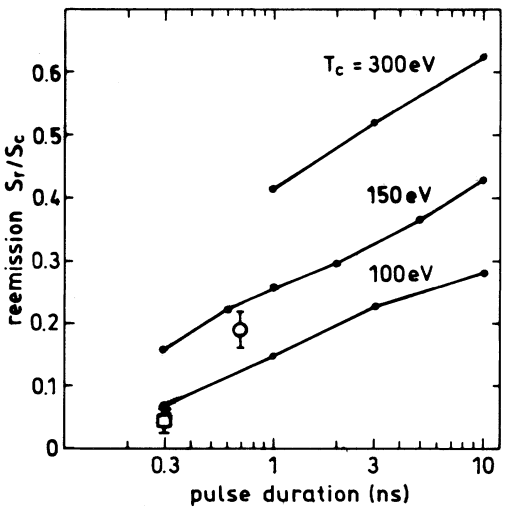

FIG. 14. Carbon reemission versus the pulse duration (FWHM) of the cavity flux. Numerical simulations at different drive temperatures carried out with sin^2 pulses. The experimental points are obtained with the Gekko XII laser heating the TC cavity (dot) and with the Asterix IV laser heating a spherical target (square).

The experimental results are in good agreement with hydrodynamic code simulations, which are based on a multigroup radiation diffusion approximation and on realistic carbon opacities. Important for the observed radiative burnthrough is the opacity between the prominent heliumlike and hydrogenlike carbon lines due to the overlapping line wings that determines the Rosseland mean opacity. Electron impact broadening was assumed to be the dominant mechanism for the conditions here. Remaining discrepancies are attributed to idealizations used in the model such as the use of an isotropic Planckian cavity flux for heating the foils. The good agreement between the theory and the experiment has motivated us to extend the model predictions to cavity fluxes with higher temperatures and longer durations, which are relevant to indirectly driven ICF. With 10-ns pulses at a drive temperature of 300 eV, the model predicts a burnthrough depth of 0.4 mm (40 mg/cm^2) and a reemission of 63%. The carbon reemission becomes high for high temperatures and long pulses because the heated layer becomes optically thick, connected with the trend to emit Planckian radiation.

ACKNOWLEDGMENTS

We would like to acknowledge the contributions of many people of MPQ and ILE in fabricating the targets and in running the Gekko laser. We would also like to thank C. Iglesias for providing us his OPAL opacity data for carbon. This work was supported in part by the commission of the European Communities in the framework of the Euratom-IPP Association, the Japan Society for the Promotion of Science, and the Monbusho International Science Program.

APPENDIX

In this appendix we discuss the question how close the radiatively heated samples are to LTE. At sufficiently high densities LTE is warranted by frequent electron collisions. The typical electron densities of the carbon sample are for this experiment in the range of a few times 10^{22} cm^{-3}. From the usual criteria for LTE (see, for ex-

ample, Ref. [44]) we find for these densities at the temperatures of this experiment that the carbon plasma is just in the transition region from LTE to non-LTE. Thus a LTE model should overestimate the ionization. On the other hand, the plasma is in contact with the intense cavity radiation field with a temperature slightly exceeding the matter temperature of the sample. For the present conditions one finds that the rates for photoexcitation or ionization are of the same magnitude as, or even larger than, the corresponding electronic rates.

We have checked the influence of the radiation by means of the RATION code [45], which is a non-LTE code including photoexcitation and ionization due to a Planckian radiation field with a radiation temperature T_c different from the matter temperature T_m. We considered the following characteristic case: $\rho=0.1$ g/cm^3 (electron density 3×10^{22}), $T_m=120$ eV, and $T_c=150$ eV. The results of RATION are given in Table IV, where we plotted the fractional populations of several carbon levels for the cases LTE and non-LTE with the radiation temperature switched on and off. It is seen that deviations from LTE under the influence of the radiation field are present. The hydrogenlike level population has increased up to approximately 10%, whereas the heliumlike level populations decreased. Thus a more accurate calculation should consider the influence of the radiation field by a non-LTE model. Nevertheless, it is seen that the deviations from LTE are tolerable and the assumption of LTE used for the simulations is not unreasonable.

TABLE IV. Fractional populations of some carbon levels according to the RATION code for different states of the plasma: LTE and non-LTE with the cavity radiation field with temperature T_c switched on and off.

Level	LTE	non-LTE $T_c=0$	non-LTE $T_c=150$ eV
C^{6+}	0.55	0.53	0.60
$C^{5+}(1s)$	0.21	0.22	0.16
$C^{5+}(2p)$	0.040	0.040	0.043
$C^{5+}(3p)$	0.050	0.050	0.053
$C^{4+}(1s^2)$	0.0095	0.010	0.0057
$C^{4+}(1s2p)$	0.0020	0.0022	0.0015

[1] P. D. Goldstone, S. R. Goldman, W. C. Mead, J. A. Cobble, G. L. Stradling, R. H. Day, A. Hauer, M. C. Richardson, R. S. Marjoribanks, P. A. Jaanimagi, R. L. Keck, F. J. Marshall, W. Seka, O. Barnouin, B. Yaakobi, and S. A. Letzring, Phys. Rev. Lett. **59**, 56 (1987).

[2] W. C. Mead, E. K. Stover, R. L. Kauffman, H. N. Kornblum, and B. F. Lasinski, Phys. Rev. A **38**, 5275 (1988).

[3] P. Celliers and K. Eidmann, Phys. Rev. A **41**, 3270 (1990).

[4] H. Nishimura, H. Takabe, K. Kondo, H. Shiraga, K. Sugimoto, T. Nishikawa, Y. Kato, and S. Nakai, Phys. Rev. A **43**, 3073 (1991).

[5] D. R. Kania, H. Kornblum, B. A. Hammel, J. Seely, C. Brown, U. Feldman, G. Glendinning, P. Young, E. Hsieh, M. Hennesian, L. DaSilva, B. J. MacGowan, D. S. Montgomery, C. A. Back, R. Doyas, J. Edwards, and R. W. Lee, Phys. Rev. A **46**, 7853 (1992).

[6] H. Nishimura, Y. Kato, H. Takabe, T. Endo, K. Kondo, H. Shiraga, S. Sakabe, T. Jitsuno, M. Takagi, S. Nakai, R. Sigel, G. D. Tsakiris, J. Massen, M. Murakami, F. Lavarenne, R. Fedosejevs, J. Meyer-ter-Vehn, K. Eidmann, and S. Witkowski, Phys. Rev. A **44**, 8323 (1991).

[7] R. L. Kauffman, L. J. Suter, C. D. Darrow, J. D. Kilkenny, H. N. Kornblum, D. S. Montgomery, D. W. Phillion, M. D. Rosen, A. R. Theissen, R. J. Wallace, and F. Ze, Phys. Rev. Lett. **73**, 2320 (1994).

[8] R. E. Marshak, Phys. Fluids **1**, 24 (1958).

[9] R. Pakula and R. Sigel, Phys. Fluids **28**, 232 (1985); **29**, 1340(E) (1986).

[10] N. Kaiser, J. Meyer-ter-Vehn, and R. Sigel, Phys. Fluids B **1**, 1747 (1989).

[11] L. B. DaSilva, B. J. MacGowan, D. R. Kania, B. A. Hammel, C. A. Back, E. Hsieh, R. Doyas, C. A. Iglesias, F. J. Rogers, and R. W. Lee, Phys. Rev. Lett. **69**, 438 (1992).

[12] P. T. Springer, D. J. Fields, B. G. Wilson, J. K. Nash, W. H. Goldstein, C. A. Iglesias, F. J. Rogers, J. K. Swenson, M. H. Chen, A. Bar-Shalom, and R. E. Stewart, Phys. Rev. Lett. **69**, 3735 (1992).

[13] Th. Löwer, R. Sigel, K. Eidmann, I. B. Földes, S. Hüller, J. Massen, G. D. Tsakiris, S. Witkowski, W. Preuss, H. Nishimura, H. Shiraga, Y. Kato, S. Nakai, and T. Endo, Phys. Rev. Lett. **72**, 3186 (1994).

[14] R. Cauble, D. W. Phillion, T. J. Hoover, N. C. Holmes, C. D. Kilkenny, R. W. Leeaanimagi, and Y. T. Lee, Phys. Rev. Lett. **70**, 2102 (1993).

[15] E. Storm, J. Fusion Energy **7**, 131 (1988).

[16] M. Murakami and J. Meyer-ter-Vehn, Nucl. Fusion **31**, 1315 (1991).

[17] R. Sigel, G. D. Tsakiris, F. Lavarenne, J. Massen, R. Fedosejevs, J. Meyer-ter-Vehn, M. Murakami, K. Eidmann, S. Witkowski, H. Nishimura, Y. Kato, H. Takabe, T. Endo, K. Kondo, H. Shiraga, S. Sakabe, T. Jitsuno, M. Takagi, C. Yamanaka, and S. Nakai, Phys. Rev. Lett. **65**, 587 (1990).

[18] R. Sigel, G. D. Tsakiris, F. Lavarenne, J. Massen, R. Fedosejevs, K. Eidmann, J. Meyer-ter-Vehn, M. Murakami, S. Witkowski, H. Nishimura, Y. Kato, H. Takabe, T. Endo, K. Kondo, H. Shiraga, S. Sakabe, T. Jitsuno, M. Takagi, C. Yamanaka, and S. Nakai, Phys. Rev. A **45**, 3987 (1992).

[19] V. J. L. White, J. M. Foster, J. C. V. Hansom, P. A. Rosen, and S. J. Rose, Phys. Rev. E **49**, R4803 (1994).

[20] B. A. Hammel, D. R. Kania, F. Rogers, C. A. Iglesias, R. W. Lee, J. F. Seely, C. M. Brown, and J. M. Edwards, Europhys. Lett. **20**, 319 (1992).

[21] W. Schwanda and K. Eidmann, Phys. Rev. Lett. **69**, 3507 (1992).

[22] S. J. Davidson, J. M. Foster, C. C. Smith, K. A. Warburton, and S. J. Rose, Appl. Phys. Lett. **52**, 847 (1988).

[23] J. Bruneau, A. Decoster, D. Desenne, H. Dumont, J. P. LeBreton, M. Boivineau, J. P. Perrine, S. Bayle, M.

Louis-Jaquet, J. P. Geindre, C. Chenais-Popovics, and J. C. Gauthier, Phys. Rev. A **44**, R832 (1991).
[24] J. Edwards, M. Dunne, D. Riley, R. Taylor, and O. Willi, Phys. Rev. Lett. **67**, 3780 (1991).
[25] J. Edwards, M. Dunne, R. Taylor, O. Willi, C. A. Back, and S. J. Rose, Phys. Rev. Lett. **71**, 3477 (1993).
[26] H. Nishimura, H. Shiraga, H. Takabe, Y. Kato, S. Miyamoto, M. Takagi, T. Norimatsu, T. Yamanaka, T. Jitsuno, M. Nakatsuka, S. Nakai, T. Endo, M. Murakami, T. Kanabe, and C. Yamanaka, in *Proceedings of the XIVth International Conference on Plasma Physics and Controlled Nuclear Fusion Research, Würzburg, 1992* (IAEA, Vienna, 1993), Vol. 3, p. 97.
[27] I. B. Földes, K. Eidmann, Th. Löwer, J. Massen, R. Sigel, G. D. Tsakiris, S. Witkowski, H. Nishimura, T. Endo, H. Shiraga, M. Takagi, Y. Kato, and S. Nakai, Phys. Rev. E **50**, R690 (1994).
[28] I. B. Földes, K. Eidmann, R. Sigel, and G. D. Tsakiris, SPIE Proc. **2015**, 179 (1994).
[29] J. Massen, G. D. Tsakiris, K. Eidmann, I. B. Földes, Th. Löwer, R. Sigel, S. Witkowski, H. Nishimura, T. Endo, H. Shiraga, M. Takagi, Y. Kato, and S. Nakai, Phys. Rev. E **50**, 5130 (1994).
[30] G. D. Tsakiris, SPIE Proc. **1032**, 910 (1989).
[31] W. Maixner, Diplomarbeit, Fachhochschule München, 1992 (unpublished).
[32] R. Sigel, in *Handbook of Plasma Physics,* edited by M. N. Rosenbluth and R. Z. Sagdeev (North-Holland, Amsterdam, 1991), Vol. 3, pp. 163–197.
[33] R. Ramis and J. Meyer-ter-Vehn, in *Laser Interaction with Matter,* Proceedings of the 23rd European Conference, Oxford, 1994, edited by S. J. Rose, IOP Conf. Proc. No. 140 (Institute of Physics and Physical Society, Bristol, 1995), p. 97.
[34] Los Alamos National Laboratory Report No. LALP-83-4, 1983 (unpublished).
[35] Th. Löwer, Dissertation, Universität Frankfurt, 1994 (unpublished); Max-Planck Institut für Quantenoptik, Report No. MPQ-192, 1994 (unpublished).
[36] B. L. Henke, P. Lee, T. J. Tanaka, R. L. Shimabukuro, and B. K. Fujikawa, At. Data Nucl. Data Tables **27**, 1 (1982).
[37] K. Eidmann, W. Schwanda, I. Földes, R. Sigel, and G. D. Tsakiris, J. Quant. Spectrosc. Radiat. Transfer **51**, 77 (1994).
[38] A. Rickert, J. Quant. Spectrosc. Radiat. Transfer **54**, 325 (1995).
[39] R. Ramis, R. F. Schmalz, and J. Meyer-ter-Vehn, Comput. Phys. Commun. **49**, 475 (1988).
[40] K. Eidmann, Laser Part. Beams **12**, 223 (1994).
[41] H. R. Griem, Phys. Rev. A **165**, 258 (1968).
[42] F. J. Rogers, C. A. Iglesias, and B. G. Wilson, Astrophys. J. **397**, 717 (1992).
[43] A. Rickert, K. Eidmann, J. Meyer-ter-Vehn, F. J. D. Serduke, and C. A. Iglesias, Max-Planck-Institut für Quantenoptik Report No. MPQ 204, 1995 (unpublished); compare Ref. [38].
[44] H. R. Griem, *Plasma Spectroscopy* (McGraw-Hill, New York, 1964).
[45] The RATION computer code was developed by R. W. Lee, Lawrence Livermore National Laboratory, Livermore, CA.

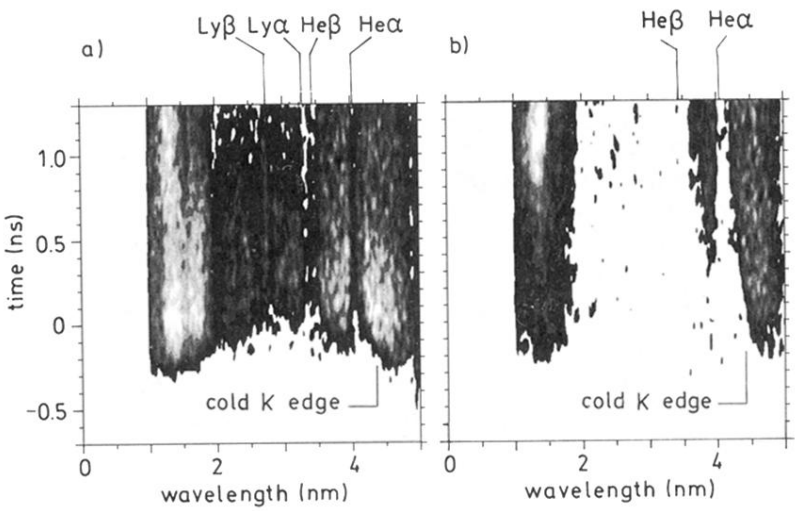

FIG. 3. Time-dependent absorption spectra of (a) 0.52-mg/cm^2 and (b) 0.79-mg/cm^2 CH foils measured with the TC cavity. The data are cut at $\lambda < 10$ Å, the region perturbed by zeroth-order contributions from the transmission grating spectrometer.

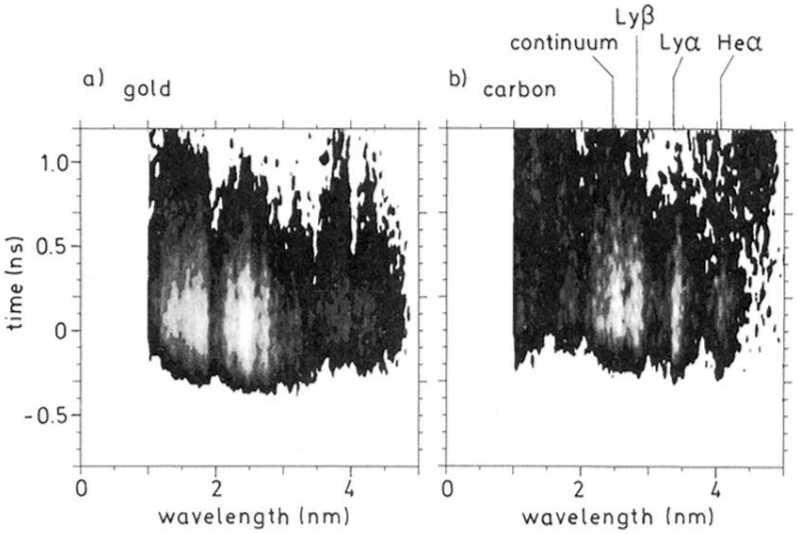

FIG. 6. Time-dependent reemission spectra measured with the TC cavity. Emission from (a) a gold wall element and (b) a carbon wall element. In (b) the XRSC sensitivity is higher by a factor 3.